Excited-State Distortions of Cyclometalated Ir(III) Complexes Determined from the Vibronic Structure in Luminescence Spectra

Xianghuai Wang,[†] Jian Li,[‡] Mark E. Thompson,*[,‡] and Jeffrey I. Zink*[,†]

Department of Chemistry and Biochemistry, University of California, Los Angeles, California 90095, and the Department of Chemistry, University of Southern California, Los Angeles, California 90089

Received: January 22, 2007; In Final Form: January 30, 2007

The luminescence spectra of $[(tpy)_2Ir(CN\text{-}t\text{-}Bu)_2](CF_3SO_3)$ in methylcyclohexane glass and frozen *n*-nonane at 15 K reveal well-resolved vibronic fine structure. The vibronic peaks are assigned by comparison with the vibrational frequencies obtained from Raman and IR spectra and those obtained using DFT electronic structure calculations. The magnitudes of the distortions along the normal coordinates are calculated by fitting the emission spectra using the time-dependent theory of spectroscopy. Broadening effects and the MIME frequency observed at room temperature are interpreted. The most highly distorted normal modes involve atomic motions on the *tpy* ligand, consistent with the metal to ligand/ligand centered assignment of the electronic transition.

Introduction

Cyclometalated Ir(III) complexes are widely used as emissive dopants in organic light emitting devices.[1−3] Spectroscopic studies have shown that the lowest excited state, which dominates the luminescence properties of cyclometalated Ir(III) complexes, is a mixture of a ligand-centered (^{3}LC) state and a metal-to-ligand-charge-transfer (^{1}MLCT) state.[4,5] The singlet and triplet electronic states mixture resulting from spin−orbit coupling reduces the luminescence lifetime and increases efficiency. The influence of the ancillary ligand LX in a series of $(tpy)_2Ir(LX)$ complexes (*tpy* = N,C$^{2'}$-(2′-*para*-tolylpyridyl)) on the ^{1}MLCT to ^{3}LC mixture has been reported.[6] In the luminescence spectra of these compounds, strong vibronic side peaks were found at lower energies than the main peak. The side peaks degrade the color quality of the OLEDs for use as display screen pixels. An ideal pixel should give a pure, saturated color, but the emission is spread over a range of wavelengths because of the vibronic progressions leading to an unsaturated color, not suitable for use as a display pixel.

A powerful method for investigating the excited-state distortions that produce the vibronic structure in an electronic spectrum is resonance Raman (rR) spectroscopy.[7−11] The intensities of the bands in the rR spectrum are used to calculate the distortions of the molecule in the resonant excited state. This type of analysis is difficult or impossible to carry out in strongly emitting molecules because the intense luminescence obscures the weaker Raman scattering. Furthermore, in the $(tpy)_2Ir(LX)$ complexes, the absorption band of the lowest-energy excited-state appears as a weak shoulder on intense fully allowed bands at slightly higher energy. The rR intensities carry information about multiple states, and in addition both constructive and destructive interference effects occur, further complicating the analysis of the excited-state distortions.[12,13]

Detailed information about excited-state distortions can be obtained directly from the electronic spectra if the vibronic structure in the spectra is highly enough resolved. Room-temperature luminescence spectra of the $(tpy)_2Ir(LX)$ compounds show what superficially appears to be a progression in a single mode. As discussed in this paper, this interpretation is misleading. Higher resolution is needed for detailed analysis, but highly resolved structure in the electronic spectra of large molecules in condensed media is uncommon.

In this paper, we report the observation that the emission spectrum of $[(tpy)_2Ir(CN\text{-}t\text{-}Bu)_2](CF_3SO_3)$ in an alkane matrix at 15 K reveals sharp vibronic structure. The spectra of this molecule in hydrocarbon glasses and as crystals at low temperature are also investigated. The vibronic structure is assigned, and the excited-state distortions are calculated using the time-dependent theory of spectroscopy. The largest distortions occur along *tpy* ligand-centered normal coordinates and are compared to those calculated by DFT electronic structure calculations. The single regularly spaced progression in the room-temperature spectrum arises from the MIME (missing mode effect).[14−16] The MIME frequency is explained and calculated. The loss of resolution as the solvent is changed or the temperature raised is reproduced by increasing the phenomenological damping factor. Finally, the vibronic structure in the emission spectrum of a sister compound, $(tpy)_2Ir(PPh_2CH_2)BPh_2$, is examined. Although the resolution was never as good as that in the CN−t-Bu complex under any of the conditions tested, we show that the distortions calculated for the *tpy* ligand in the latter complex can be transferred to the system complex and an excellent fit to the spectrum is obtained. This result is consistent with the interpretation that the distortions in the mixed *tpy* ligand-centered ^{3}LC and the metal to *tpy* charge transfer state are dominated by the *tpy* ligand and only weakly perturbed by the ancillary ligand.

Experimental Section

Compounds. $[(tpy)_2Ir(CN\text{-}t\text{-}Bu)_2](CF_3SO_3)$ and $(tpy)_2Ir(PPh_2CH_2)BPh_2$ were synthesized using literature methods.[6] Reagent-grade *n*-nonane (99%), toluene (99.5%), and spectrophotometric-grade methylcyclohexane (99%) were purchased from Aldrich Chemical Co. and used as received.

Emission Spectroscopy. The room-temperature emission spectra of $[(tpy)_2Ir(CN\text{-}t\text{-}Bu)_2](CF_3SO_3)$ and $(tpy)_2Ir(PPh_2CH_2)$-

* Authors to whom correspondence should be addressed. E-mail: mthompso@usc.edu; zink@chem.ucla.edu.
† University of California, Los Angeles.
‡ University of Southern California.

10.1021/jp0705525 CCC: $37.00
Published on Web 04/10/2007

BPh_2 in toluene were excited at 350 nm and recorded by a Fluorolog FL 3-22 (Jobin-Yvon/ISA Spex). Low-temperature emission spectra (15K) were obtained from samples in capillary tubes cooled by an Air Products closed cycle helium refrigerator displex. A Spex 1702 single monochromator equipped with an S1 photomultiplier tube was used to collect the signal, which was recorded by a Stanford Research System SR400 photon counter and processed by a computer. The 350.7 nm line (5 mW) from a Coherent I-300 Krypton ion laser was used for excitation. The emission spectra were recorded with 1 Å resolution. The spectra shown are the average of nine individual spectra.

Vibrational Spectroscopy. Raman spectra were recorded by a Jobin-Yvon HR 640 triple monochromator equipped with a CCD. The 647.1 nm line of a Coherent I-300 Krypton ion laser (50 mW) was used for excitation. The sample was mixed with KNO_3 as the internal standard (1:5 weight ratio) and pressed into a pellet. Infrared spectra were taken of the samples in KBr pellets on a Jasco model 420 FTIR spectrometer with a 4 cm^{-1} resolution.

Theoretical Methods

Time-Dependent Theory. The theoretical background needed to calculate the emission spectra is briefly presented in this section. The time-dependent theory is used because it is powerful from both technique and conceptual points of view.[7,17−24] The fundamental equation for the calculation of an emission spectrum in the time-dependent theory is

$$I(\omega) = C\omega^3 \int_{-\infty}^{+\infty} \exp(i\omega t)\left\{\langle\Phi|\Phi(t)\rangle \exp\left(-i\frac{E_0}{h}t - \Gamma^2 t^2\right)\right\} \mathrm{d}t \quad (1)$$

where C is a constant, $I(\omega)$ is the intensity in photons per unit volume per unit time at frequency ω, E_0 is the energy difference between the minima of the excited-state and ground state, and Γ is a damping factor.[7] The damping factor Γ arises because of relaxation into other modes and the "bath". Increasing Γ will result in decreasing the spectrum resolution, that is, only broad peaks can be seen on the emission spectrum.

In eq 1, the total autocorrelation function $\langle\Phi|\Phi(t)\rangle$ is the overlap of the initial wave packet, Φ, with the time-dependent wave packet, $\Phi(t)$. The total overlap in a system with K coordinates is given by

$$\langle\Phi|\Phi(t)\rangle = \prod_k \langle\phi_k|\phi_k(t)\rangle \quad (2)$$

where ϕ_k is a wave packet associated with normal mode coordinate k ($k = 1,..., K$).

The propagating wave packet $\phi_k(t)$, which in the initial wave packet propagates on the destination potential surface, is the most important quantity in the calculation and can be calculated by time-dependent Schrödinger equation:

$$i\frac{\partial\phi_k(t)}{\partial t} = \hat{H}_k\phi_k(t) \quad (3)$$

where $\hat{H}_k = -(1/2m_k)\nabla^2 + V(Q_k)$, $V(Q_k)$ is the potential energy as a function of the configurational coordinate Q_k, and $-(1/2m_k)\nabla^2$ is the kinetic energy. The propagating wave packet $\phi_k(t)$ is calculated by the split operator method,[25] in which both the coordinate Q_k and the time t are represented by grid points which have the interval ΔQ_k and Δt, respectively. Thus, the time-dependent wavefunction $\phi(Q_k, t + \Delta t)$ can be obtained from $\phi(Q_k, t)$ using the equation

$$\phi_k(Q_k, t + \Delta t) = \exp\left(\left(\frac{i\Delta t}{4m_k}\right)\nabla^2\right)\exp(i\Delta t V)\exp\left(\left(\frac{i\Delta t}{4m_k}\right)\nabla^2\right)\phi_k(Q_k, t) + O[(\Delta t)^3] = \hat{P}\hat{V}\hat{P}\phi_k(Q_k, t) + O[(\Delta t)^3] \quad (4)$$

However, a simple form of the overlap $\langle\phi_k|\phi_k(t)\rangle$ can be obtained[7] if the potential surfaces are harmonic, there is no change in the force constants between the ground and excited states, and the transition dipole moment is a constant (Condon approximation). Then

$$\langle\phi_k|\phi_k(t)\rangle = \exp\left\{-\frac{\Delta_k^2}{2}(1 - \exp(-i\omega_k t)) - \frac{i\omega_k t}{2}\right\} \quad (5)$$

where ω_k is the vibrational frequency in cm^{-1} and Δ_k is the displacement of the kth normal mode.

DFT Calculation. Optimized geometries and vibrational modes are calculated by the DFT method, which is performed using the Jaguar quantum chemistry program.[26] The BP86 functional is used. This functional includes the Slater local exchange functional,[27] Becke's 88 nonlocal gradient correction to exchange,[28] and Perdew's gradient correction functional[29,30] for the Vosko−Wilk−Nusair(VWN) local correlation functional.[31] The LACVP** basis set[32] is employed. It has an effective core potential (ECP) for Ir and uses 6-31G** for H, C, and N atoms.

Results

Room-Temperature Emission Spectra. The room-temperature emission spectrum of $[(tpy)_2Ir(CN\text{-}t\text{-}Bu)_2](CF_3SO_3)$ in toluene is shown in Figure 1a. The spectrum contains two resolved peaks at 21 690 and 20 280 cm^{-1} and a shoulder at about 19 000 cm^{-1}. The emission spectrum of $(tpy)_2Ir(PPh_2CH_2)BPh_2$ in toluene is shown in Figure 1b. Its spectrum contains two resolved peaks at 21 230 and 19 880 cm^{-1} and a shoulder at about 18 500 cm^{-1}.

Low-Temperature Emission Spectra. The emission spectra of $[(tpy)_2Ir(CN\text{-}t\text{-}Bu)_2](CF_3SO_3)$ in *n*-nonane at 15K (10^{-6} mol/L) is shown in Figure 2a and that of $[(tpy)_2Ir(CN\text{-}t\text{-}Bu)_2](CF_3SO_3)$ in methylcyclohexane in Figure 2b. Both show highly resolved vibronic structure. The emission spectrum in Figure 2b is more highly resolved and exhibits low-frequency structure that is magnified in the insert in Figure 2b. The intervals between the peaks in the insert are about 30 cm^{-1}, and the full-width-half-maxima (fwhm) of those peaks are about 18 cm^{-1}. The wavenumber difference between the highest-wavenumber peak and other peaks is listed in Table 1. The spectra were taken at 1 Å resolution, which is about 6 cm^{-1} in the region of 401.6−406.5 nm in Figure 2b and are the average of nine runs. The uncertainty in the peak position is ~6 cm^{-1}, and that in the peak height is ±5%.

The emission spectrum of $(tpy)_2Ir(PPh_2CH_2)BPh_2$ in *n*-nonane at 15K is shown in Figure 2c. This spectrum is not as well resolved as those in Figure 2a,b, but it does contain poorly resolved vibronic features. The wavenumber separation between the two main peaks is 1482 cm^{-1}.

Vibrational Spectra. The vibrational modes of $[(tpy)_2Ir(CN\text{-}t\text{-}Bu)_2](CF_3SO_3)$ found in the Raman spectra below 1800 cm^{-1} are 333, 440, 655, 675,727, 841, 976, 1035, 1118, 1138, 1160, 1204, 1228, 1266, 1300, 1313, 1364, 1476, 1549, 1558, 1585, and 1603 cm^{-1}. The vibrational modes of $[(tpy)_2Ir(CN\text{-}t\text{-}Bu)_2]$-

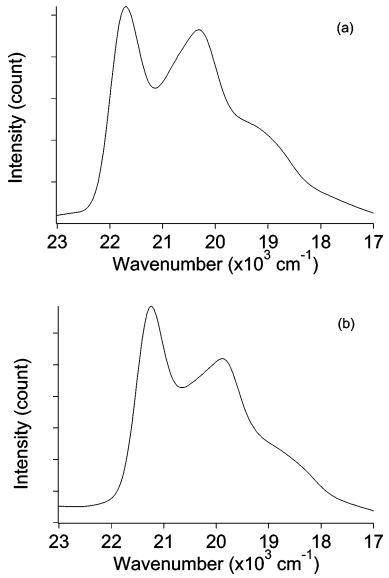

Figure 1. (a) Emission spectra of $[(tpy)_2Ir(CN\text{-}t\text{-}Bu)_2](CF_3SO_3)$ in toluene excited at 351 nm at room temperature. (b) Emission spectra of $(tpy)_2Ir(PPh_2CH_2)BPh_2$ in toluene excited at 351 nm at room temperature.

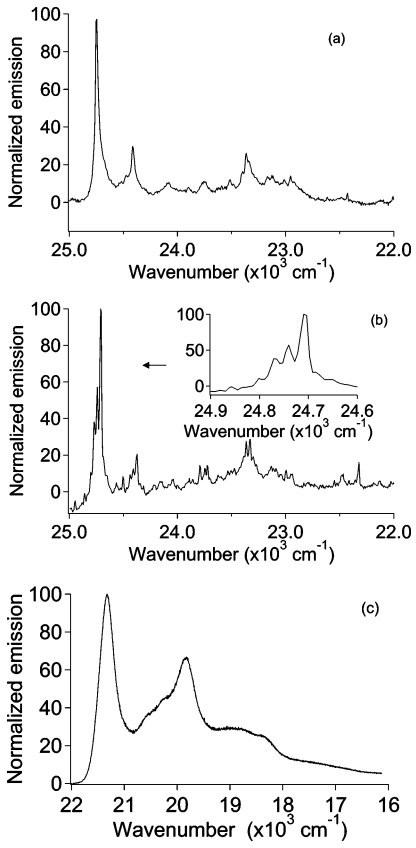

Figure 2. (a) Emission spectrum of $[(tpy)_2Ir(CN\text{-}t\text{-}Bu)_2](CF_3SO_3)$ in methylcyclohexane excited at 351 nm at 15 K. (b) Emission spectrum of $[(tpy)_2Ir(CN\text{-}t\text{-}Bu)_2](CF_3SO_3)$ in *n*-nonane excited at 351 nm at 15 K. The band origin of the emission spectrum is magnified to show the fine structure. (c) Emission spectrum of $(tpy)_2Ir(PPh_2CH_2)BPh_2$ *n*-nonane excited at 351 nm at 15 K.

(CF_3SO_3) found in the Raman spectrum that play a major role in the discussion of the luminescence spectra are listed in Table 2. IR peaks of $[(tpy)_2Ir(CN\text{-}t\text{-}Bu)_2](CF_3SO_3)$ below 1800 cm^{-1} are observed at 317, 333, 345, 365, 381, 423, 439, 512, 524, 565, 632, 673, 717, 749, 774, 815, 847, 874, 957, 1025, 1062, 1150, 1187, 1219, 1266, 1317, 1374, 1400, 1428, 1462, 1476, 1558, 1585, and 1603 cm^{-1}.

TABLE 1: Positions of the Peaks in the Emission Spectrum of $[(tpy)_2Ir(CN\text{-}t\text{-}Bu)_2](CF_3SO_3)$ in Methylcyclohexane

position (cm^{-1})	diff (cm^{-1})	assignment
24746	0	E_{00}
24414	332	δ_1
24079	667	$2\delta_1$, δ_2, δ_3[a]
24027(sh)	719	δ_4
23895	851	δ_5
23753	993	δ_6
23590	1156	δ_7
23513	1233	δ_8
23480	1266	δ_9
23397	1349	δ_{10}
23364	1382	δ_{11}
23277(sh)	1469	δ_{12}
23170	1576	δ_{13}
23127	1619	δ_{14}
23010	1736	$\delta_{11}+\delta_1$
22952	1794	$\delta_{12}+\delta_1$

[a] Three modes are needed to fit the intensity.

The 40 most intense Raman bands in the spectrum of $(tpy)_2Ir(PPh_2CH_2)BPh_2$ are observed at 265, 295, 339, 373, 508, 520, 528, 577, 595, 619, 656, 679, 733, 748, 812, 847, 877, 1001, 1017, 1034, 1068, 1082, 1098, 1120, 1141, 1159, 1188, 1207, 1226, 1242, 1269, 1304, 1318, 1373, 1385, 1480, 1553, 1584, 1589, and 1611 cm^{-1}.

Discussion

The unusual observation of highly resolved vibronic structure in the emission spectrum of a large transition metal complex enables an analysis of the excited-state distortions to be made. The best results were obtained with $[(tpy)_2Ir(CN\text{-}t\text{-}Bu)_2](CF_3SO_3)$ in frozen nonane. A long-chain alkane matrix containing a low concentration of a luminescent molecule and cooled down to cryogenic temperatures is known as a Shpol'skii matrix.[33] The first examples of highly resolved emission spectra in Shpol'skii matrices were obtained from aromatic hydrocarbons in n-paraffins (*n*-hexane, *n*-pentane, etc.). Such systems have been widely used to obtain narrow spectral lines from planar aromatic hydrocarbons.[34−37] In a recent study, sharp line vibronic structure from a planar organometallic compound in a Shpol'skii matrix was reported.[38] It is surprising that an octahedral organometallic ion can be incorporated in a Shpol'skii matrix.

We begin our discussion with the assignments of vibrational modes that contribute to the peaks in the emission spectrum based on DFT calculations. We then use time-dependent theory to calculate the magnitudes of the distortions, explain them in terms of the metal to ligand charge transfer, and relate them to bond length changes obtained from the DFT calculations. We briefly analyze the low-frequency vibronic structure caused by the matrix. The broadening of the spectra by the "bath" (including frozen organic glass at low temperature) and by raising the temperature are calculated, and the MIME is analyzed. Finally, we show that the spectrum of $(tpy)_2Ir(PPh_2CH_2)BPh_2$ can be fit using *tpy* ligand distortions calculated from the spectrum of $[(tpy)_2Ir(CN\text{-}t\text{-}Bu)_2](CF_3SO_3)$.

1. Assignment of Vibrations. The vibrational analysis was done by using DFT calculations, and the vibration frequencies were viewed using the MOLDEN[39] software package for identifying vibrational motions. The calculated frequencies and assignments of modes important in the vibronic structure are

TABLE 2: Vibration Frequencies and Distortions Used in Fitting the Emission Spectrum of $[(tpy)_2Ir(CN\text{-}t\text{-}Bu)_2](CF_3SO_3)$ in Methylcyclohexane

vibrational mode (cm^{-1})	assignment	IR/Raman	vibrational mode (cm^{-1}) (calcd)	distortion
333	δ_1	Raman	332 (*tpy* ring in plane bend and Ir-N stretch)	0.8
654	δ_2	Raman	665 (*tpy* ring in plane bend)	0.3
679	δ_3	IR, Raman	714 (*tpy* ring out of plane bend)	0.25
727	δ_4	Raman	737 (*tpy* ring out of plane bend)	0.25
841	δ_5	IR, Raman	858 (*tpy* ring out of plane bend)	0.35
976	δ_6	Raman	984 (*tpy* ring stretch)	0.45
1138	δ_7	Raman	1158 (*tpy* ring stretch)	0.4
1228	δ_8	Raman	1247 (*tpy* ring stretch)	0.5
1266	δ_9	IR, Raman	1310 (*tpy* ring stretch)	0.3
1354	δ_{10}	Raman	1377 (*tpy* ring stretch)	0.4
1400	δ_{11}	IR	1427 (*tpy* ring stretch)	0.75
1476	δ_{12}	IR, Raman	1483 (*tpy* ring stretch)	0.5
1585	δ_{13}	IR, Raman	1599 (*tpy* ring stretch)	0.3
1603	δ_{14}	IR, Raman	1612 (*tpy* ring stretch)	0.5

SCHEME 1

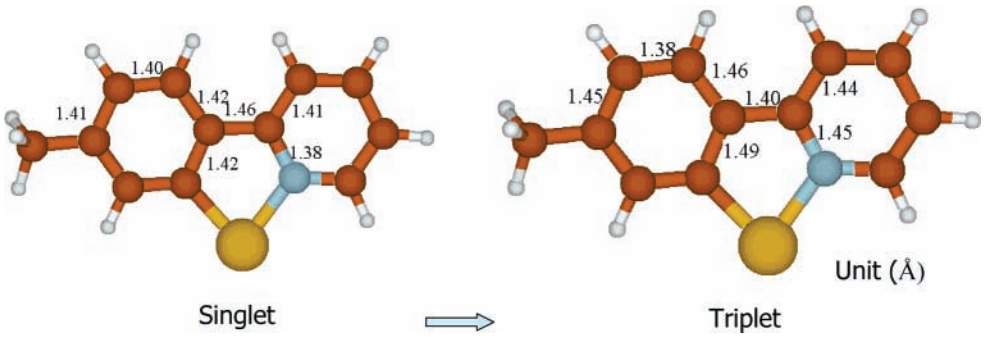

listed in the fourth column of Table 2. These vibrational motions all involve C−C/C−N *tpy* ligand bond stretching.

2. Low-Temperature Emission Spectra and Calculation of Distortions. The emission spectrum of $[(tpy)_2Ir(CN\text{-}t\text{-}Bu)_2](CF_3SO_3)$ about 10^{-6} M in methylcyclohexane at 20K is shown in Figure 2b. The assignment of the peaks is based on the measured vibrational frequencies obtained from the IR and Raman spectra; these frequencies are listed in the first column of Table 2.

The emission spectrum is fit by time-dependent theory and the measured vibrational frequencies. The fitting parameters are the excited-state potential surface displacements, Δ, along each of the normal modes. Fourteen vibrational frequencies are used for the fitting. The fitting result is shown in Figure 3 and Table 2.

In our emission spectrum fitting results shown in Table 2, the 333 and 1400 cm^{-1} modes have relatively large distortions. In order to understand the physical meaning of those large distortions, we also did the DFT frequency calculation on $[(tpy)_2Ir(CN\text{-}t\text{-}Bu)_2](CF_3SO_3)$ molecule and the result shows that

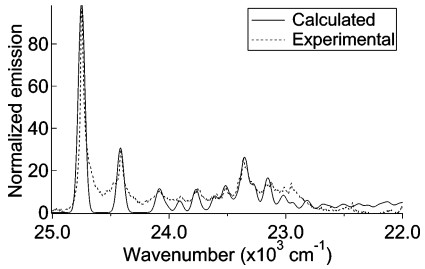

Figure 3. Emission spectrum of $[(tpy)_2Ir(CN\text{-}t\text{-}Bu)_2](CF_3SO_3)$ in methylcyclohexane at 15 K calculated by time-dependent theory. The solid line is the calculated result, and the dotted line is the experimental spectrum.

the 333 cm^{-1} vibration mode involves stretching of Ir−N and C−C bonds in the *tpy* ligand and the 1400 cm^{-1} mode is mainly C−N bond stretching in the *tpy* ligand. It also supports the assignment of the lowest excited-state as the mixture of MLCT/LC electronic states. As there is a charge transfer from Ir to the *tpy* ligand, it is expected that the bond length in the *tpy* ligand would change. Thus, those *tpy* ligand centered vibrational modes would exhibit large distortions in the lowest excited state. Our DFT calculation on the optimized geometry of lowest singlet and triplet states also shows that there is a large bond length change occurring in the *tpy* ligand. Although the lowest excited-state is a mixture of ^{1}MLCT and ^{3}LC electronic state, the calculation on the lowest triplet state structure should give an approximately correct explanation. Those bond length changes are shown in Scheme 1, where only one *tpy* ligand and the Ir atom are shown for clarity. As shown in Scheme 1, the C−C and C−N bond length change varies from 0.02 to 0.07 Å. The differences in the *tpy* bond lengths between the singlet and triplet states can be used to explain the distortions of the vibrational modes used in the fitting (with the exception of the 333 and 1400 cm^{-1} modes). The assignments of these modes based on the DFT calculations show that they involve *tpy* ligand-centered bond stretching character.

3. Analysis of the Low-Frequency Vibronic Structure. The spectrum of $[(tpy)_2Ir(CN\text{-}t\text{-}Bu)_2](CF_3SO_3)$ in frozen nonane is even more highly resolved than that in methylcyclohexane as shown in Figure 2a. The most obvious consequence is that the lowest energy peak (at 24 746 cm^{-1} in methylcyclohexane) is resolved into multiple peaks with a separation of 30 cm^{-1}.

Attempts to fit this low-frequency structure using a harmonic potential energy surface were unsuccessful. The intensity of the experimental peaks increases gradually but decreases suddenly whereas the harmonic potential gives rise to the usual Poisson distribution of intensities. An example of an attempted fit with

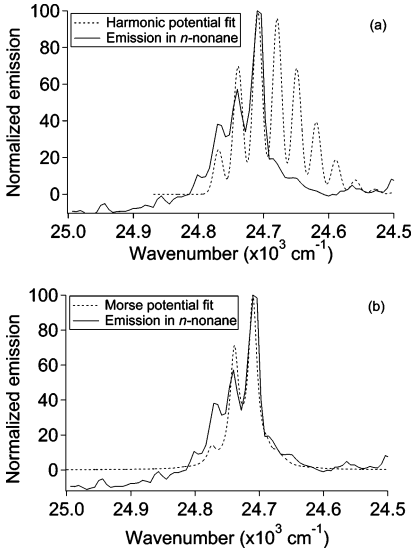

Figure 4. Calculated emission spectra of $[(tpy)_2Ir(CN\text{-}t\text{-}Bu)_2](CF_3SO_3)$ in *n*-nonane. (a) Harmonic potential fit. (b) Morse potential fit.

a harmonic potential ($\omega = 30$ cm^{-1} and $\Delta = 2.4$) is shown in Figure 4a. A Morse potential surface provides a better fit of the low-frequency structure. The Morse potential surface is given by eq 6:

$$V(r) = D_e(1 - \exp(-\beta(r - r_e)))^2 \qquad (6)$$

where r is the bond length, r_e is the equilibrium bond length (the bond length at the potential minimum), D_e is the depth of the potential well, and β is a parameter controlling the width of the potential well. The fit resulting from the Morse potential is shown in Figure 4b with parameters $D_e = 180$ cm^{-1}, $\beta = 2.78 \times 10^{-7}$ cm^{-1}, $r_e = 0$ Å of ground state, $r_e = 0.795$ Å of excited-state, and energy difference 24824 cm^{-1} between the minimum of two states. The low D_e value implies weak interaction that would not be stable at room temperature. This weak interaction that results in the low-frequency separation between the peaks is probably caused by interactions between the iridium complex and the nonane matrix molecules.

4. The Missing Mode Effect and Spectral Broadening. The spectra of $[(tpy)_2Ir(CN\text{-}t\text{-}Bu)_2](CF_3SO_3)$ provide an excellent example of the missing mode effect (MIME). In the room-temperature emission spectrum in toluene, the detailed vibronic structure is unresolved and the spectrum appears to consist of a poorly resolved progression with a spacing between the peaks of about 1400 cm^{-1}. Lowering the temperature and changing the solvent to nonane resolves features that cannot be observed in the solution spectrum as shown in Figure 5a. The resolved features can be used to quantify the MIME.

The MIME is best understood from the viewpoint of the time-dependent theory. In the time domain, two or more vibrational modes can combine to give a recurrence in the overlap at $\tau = \tau_m$ which is not possible from any one mode alone. This recurrence results in the MIME progression with a spacing of $\omega_m + 2\pi c/\tau_m$ in the frequency domain. A requirement for the appearance of the MIME is that the spectrum must not be fully resolved. The damping factor Γ must be large. When Γ is small, there will be many recurrences of the overlap in the time domain and the emission spectrum will exhibit sharp, well-defined vibronic structure. Progressions in the normal modes and combination bands will be observed. The time-dependent overlap for the calculation of the low-temperature, highly resolved nonane spectrum where $\Gamma = 20$ cm^{-1} is shown in

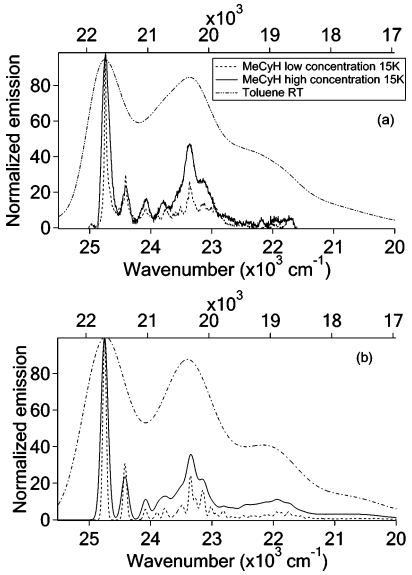

Figure 5. (a) (−••)Emission spectrum of $[(tpy)_2Ir(CN\text{-}t\text{-}Bu)_2](CF_3SO_3)$ in toluene at room temperature. (—) Higher concentration of sample ($\sim 10^{-4}$ M) in methylcyclohexane at 15 K. (---) Lower concentration of sample ($\sim 10^{-6}$ M) in methylcyclohexane at 15 K. (b) Time-dependent theory fit of the emission spectra. The vibration frequencies and normal mode distortions are listed in Table 2. (−••) $\Gamma = 230$ cm^{-1}, (—) $\Gamma = 40$ cm^{-1}, (---) $\Gamma = 20$ cm^{-1}.

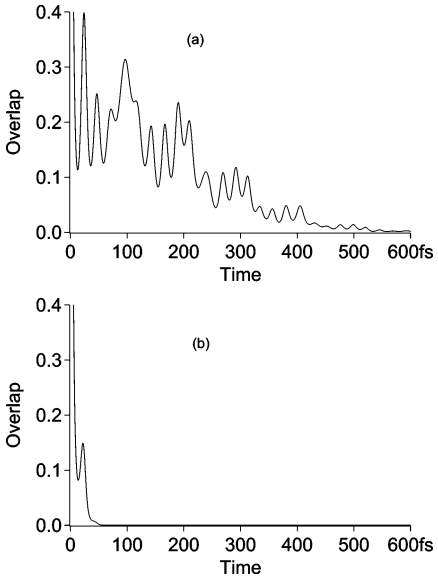

Figure 6. Time dependence of the overlap for the calculated spectra shown in Figure 5b: (a) $\Gamma = 20$ cm^{-1}, (b) $\Gamma = 230$ cm^{-1}.

Figure 6a. In this case, the overlap function contains many recurrences. When Γ is increased (to 230 cm^{-1} for example), the recurrences at long times are damped out and the spectrum is filled in. The time-dependent overlap using the same distortions as those used for Figure 5b and a Γ of 230 cm^{-1} is shown in Figure 6b. In this case, the long time recurrences are damped out, leaving only one prominent recurrence at $\tau = \tau_m = 0.0217$ ps.

The evolution of sharp vibronic structure as a function of experimental conditions is shown in Figure 5b. The most highly structured luminescence spectrum of $[(tpy)_2Ir(CN\text{-}t\text{-}Bu)_2](CF_3SO_3)$ is observed at low temperature in methylcyclohexane. At a higher concentration (10^{-4} M), the broadening is significantly larger, and at room temperature and higher concentration in toluene, only the MIME progression is observed. These emission

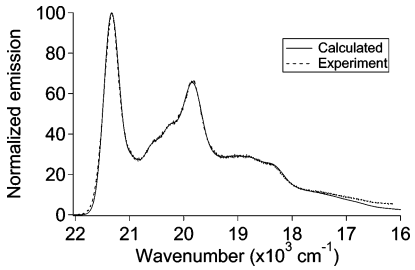

Figure 7. Emission spectra of $(tpy)_2Ir(PPh_2CH_2)BPh_2$ in *n*-nonane at 15 K. The solid line is the calculated spectrum and the dotted line is the experimental spectrum.

features can be reproduced by changing only the damping factor Γ (20, 40, and 230 cm^{-1}, respectively) as shown in Figure 5b.

5. Poorly Resolved Vibronic Structure: $(tpy)_2Ir(PPh_2CH_2)BPh_2$. The electronic structures of the iridium compounds considered in this paper are typical of many important luminophores in two common ways: the spin-forbidden emitting state lies close in energy to spin-allowed states, and the emission and absorption spectra overlap significantly. Both of these factors make it very difficult to obtain detailed resonance Raman spectroscopic information about the emitting state. The resonance Raman intensities are dominated by the allowed state and thus do not accurately measure the distortions in the emitting state. In addition, the intense luminescence swamps the weaker Raman signals. For these reasons, the applicability of the powerful resonance Raman analyses may be limited. The observation of highly resolved vibronic structure in the emission spectrum, however, enables the distortions to be determined from the electronic spectrum. Unfortunately, highly resolved emission spectra are not common; simply changing one of the ligands in the $[(tpy)_2IrL_2]$ complexes discussed in this paper from CN-t-Bu to PPH_2CH_2 drastically decreases the resolution.

It is of interest to test whether or not the detailed distortion information obtained from the spectra of $[(tpy)_2Ir(CN\text{-}t\text{-}Bu)_2](CF_3SO_3)$ can be used to obtain an estimate of the distortion of the similar $(tpy)_2Ir(PPh_2CH_2)_2BPh_2$ complex. Both the nature of the excited states and the *tpy* vibrational frequencies are very similar. Can a reasonable fit to the more poorly resolved $(tpy)_2Ir(PPh_2CH_2)_2BPh_2$ emission spectrum be obtained by using the measured vibrational frequencies and distortions in those normal modes obtained from the more highly resolved spectrum?

Using the experimental vibrational frequencies obtained from Raman spectrum and assuming that the distortions are about the same as those of modes with similar frequencies in the $[(tpy)_2Ir(CN\text{-}t\text{-}Bu)_2](CF_3SO_3)$ spectra, the emission spectrum was calculated using time dependent theory. First, exactly the same distortions for modes of frequencies similar to those of $[(tpy)_2Ir(CN\text{-}t\text{-}Bu)_2](CF_3SO_3)$ were used to calculate the emission spectrum of $(tpy)_2Ir(PPh_2CH_2)_2BPh_2$. The calculated result reproduces the coarse structure of the spectrum but did not fit all of the shoulders. Because these two molecules have different LX ligands, their ground states and excited states will be slightly different. The values of Δ were varied to obtain the excellent fit shown in Figure 7. The vibrational modes and distortions used in the calculation were: 339 (0.66), 508 (0.35), 520 (0.23), 656 (0.25), 679 (0.3), 733 (0.3), 748 (0.45), 847 (0.5), 1001 (0.37), 1034 (0.4), 1068 (0.38), 1141 (0.35), 1226 (0.54), 1269 (0.3), 1400 (0.52), 1480 (0.78), 1589 (0.4), and 1611 cm^{-1} (0.55), where the distortions are listed in the parentheses. The distortions of several of the modes with small Δ's used in the fitting are not unique, i.e., the calculated spectrum does not change significantly if the distortion of one mode is increased and another is decreased. The fit is most sensitive to modes with large distortions, especially the 339, 847, 1226, 1400, 1480 and 1611 cm^{-1} modes. These five modes, all involving the *tpy* ligand and the Ir-*tpy* bonds, also have large distortions and involve *tpy* ring stretch in the fit of the spectrum of $[(tpy)_2Ir(CN\text{-}t\text{-}Bu)_2](CF_3SO_3)$ (Table 2). These results suggest that the distortions in the *tpy* ligand and in the Ir-ligand bonds caused by populating the charge-transfer excited-state are very similar in the two compounds.

Summary

The room temperature and low-temperature emission spectra of $[(tpy)_2Ir(CN\text{-}t\text{-}Bu)_2](CF_3SO_3)$ and $(tpy)_2Ir(PPh_2CH_2)BPh_2$ are recorded in toluene, methylcyclohexane, and nonane. The emission spectra of $[(tpy)_2Ir(CN\text{-}t\text{-}Bu)_2](CF_3SO_3)$ in frozen methylcyclohexane and nonane at 15 K contain highly resolved vibronic structure. The spectra are fit using the time-dependent theory of spectroscopy. Fourteen normal modes are identified from the vibronic peaks and used in the fitting. The modes with the largest excited-state distortions, 333 cm^{-1} and 1400 cm^{-1}, are assigned to the Ir−C and *tpy* ligand C−C bond stretching and to the *tpy* ligand C−N bond stretching, respectively by using DFT calculations. A large geometry change of the *tpy* ligand between the ground state and the lowest triplet was calculated, consistent with the assignments of the modes used in the fitting of the emission spectrum. These distortions are consistent with the assignment of the lowest excited-state as a mixture of MLCT/LC electronic states.

The spectrum of $[(tpy)_2Ir(CN\text{-}t\text{-}Bu)_2](CF_3SO_3)$ in *n*-nonane at 15K contains low-frequency progressions with a separation of 30 cm^{-1}. The best fit to these peaks required the use of a Morse potential with very low energy for bond formation $D_e =$ 180 cm^{-1}. Thus, these peaks are assigned to phonon interactions between the metal complex and the molecules comprising the matrix.

The room-temperature spectrum of $[(tpy)_2Ir(CN\text{-}t\text{-}Bu)_2](CF_3SO_3)$ in methylcyclohexane and toluene contains an regularly spaced progression that does not correspond to a single vibrational normal coordinate. This result, known as the missing mode effect, is explained and calculated quantitatively from the frequencies and distortions determined from the more highly resolved spectra by increasing the phenomenological damping factor Γ.

This analysis of $(tpy)_2Ir(LX)$ compounds provides detailed information about the C−C and C−N bond distortions that result in the vibronic peaks observed to the red of the main peak. The lowest excited-state is known to be ^{3}LC-dominant. Changing the LX ligand can change the mixing of excited-state states and thus change the distortions along particular normal coordinates. The relative intensities of the vibronic peaks will change correspondingly. Decreasing the MLCT coefficient will lead to smaller distortions. This is clearly seen in comparing the dimensionless distortion Δ for complexes with a range of different LX ligands. The Δ values for a series of $(tpy)_2Ir(LX)$ complexes fall between 0.66 for LX = acetylacetone and 1.13 for the complex studied here, i.e., LX = $(CN\text{−}t\text{-}Bu)_2$.[6] A weaker mixture of MLCT states will decrease efficiency; a suitable LX ligand for device applications is one that could meet the balance between efficiency and pixel quality (small distortions).

Acknowledgment. J. I. Z. gratefully acknowledges financial support from the National Science Foundation (CHE-0507929). M. E. T. was supported by the Universal Display Corporation and the Department of Energy (DE-FC26-04NT42272).

References and Notes

(1) Baldo, M. A.; Forrest, S. R.; Thompson, M. E. In *Organic Electroluminescence*; Kafafi, Z., Ed.; Optical Engineering 94; CRC Press, Taylor & Francis: Boca Raton, FL, 2005; p 267.
(2) Lai, S.-W.; Che, C.-M. *Top. Curr. Chem.* **2004**, *241*, 27.
(3) Hughes, G.; Bryce, M. R. *J. Mater. Chem.* **2005**, *15*, 94.
(4) Colombo, M. G.; Güdel, H. U. *Inorg. Chem.* **1993**, *32*, 3081.
(5) Strouse, G. F.; Güdel, H. U.; Bertolasi, V.; Ferretti, V. *Inorg. Chem.* **1995**, *34*, 5578.
(6) Li, J.; Djurovich, P. I.; Alleyne, B. D.; Yousufuddin, M.; Ho, N. N.; Thomas, J. C.; Peters, J. C.; Bau, R.; Thompson, M. E. *Inorg. Chem.* **2005**, *44*, 1713.
(7) Zink, J. I.; Shin, K.-S. K. In *Advances in Photochemistry*; Wiley: New York, 1991; Vol. 16, p 119.
(8) Shin, K.-S. K.; Zink, J. I. *Inorg. Chem.* **1989**, *28*, 4358.
(9) Shin, K.-S. K.; Zink, J. I. *J. Am. Chem. Soc.* **1990**, *112*, 7148.
(10) Myers, A. B. In *Laser Techniques in Chemistry*; Wiley: New York, 1995; Vol. 23, p 325.
(11) Myers, A. B. *Acc. Chem. Res.* **1997**, *30*, 519.
(12) Balley, S. E.; Zink, J. I.; Nelsen, S. F. *J. Am. Chem. Soc.* **2003**, *125*, 5939.
(13) Balley, S. E.; Cohan, J. S.; Zink, J. I. *J. Phys. Chem. B* **2000**, *104*, 10743.
(14) Tutt, L.; Tannor, D.; Heller, E. J.; Zink, J. I. *Inorg. Chem.* **1982**, *21*, 3858.
(15) Tutt, L.; Tannor, D.; Schindler, J.; Heller, E. J.; Zink, J. I. *J. Phys. Chem.* **1983**, *87*, 3017.
(16) Larson, L. J.; Zink, J. I. *Inorg. Chem.* **1989**, *28*, 3519.
(17) Lee, S.-Y.; Heller, E. J. *J. Chem. Phys.* **1979**, *71*, 4777.
(18) Heller, E. J. *Acc. Chem. Res.* **1981**, *14*, 368.
(19) Heller, E. J.; Sundberg, R. L.; Tannor, D. J. *J. Phys. Chem.* **1982**, *86*, 1822.
(20) Hanna, S. D.; Zink, J. I. *Inorg. Chem.* **1996**, *35*, 297.
(21) Wootton, J. L.; Zink, J. I. *J. Phys. Chem.* **1995**, *99*, 7251.
(22) Reber, C.; Zink, J. I. *J. Chem. Phys.* **1992**, *96*, 2681.
(23) Henary, M.; Wootton, J. L.; Khan, S. I.; Zink, J. I. *Inorg. Chem.* **1997**, *36*, 796.
(24) Henary, M.; Zink, J. I. *J. Am. Chem. Soc.* **1989**, *111*, 7407.
(25) Feit, M. D.; F. J. A.; Steiger, A. *J. Comput. Phys.* **1982**, *47*, 412.
(26) *Jaguar 4.1*; Schrödinger Inc.: Portland, OR, 2000.
(27) Slater, J. C. *Quantum Theory of Molecules and Solids, The Self Consistent Field for Molecules and Solids*; McGraw-Hill: New York, 1974; Vol. 4.
(28) Becke, A. D. *Phys. Rev. A* **1988**, *38*, 3098.
(29) Perdew, J. P. *Phys. Rev. B* **1986**, *33*, 8822.
(30) Perdew, J. P. *Phys. Rev. B* **1986**, *34*, 7406.
(31) Vosko, S. H.; Wild, L.; Nusair, M. *Can. J. Phys.* **1980**, *58*, 1200.
(32) Hay, P. J.; Wadt, W. R. *J. Chem. Phys.* **1985**, *82*, 299.
(33) Shpol'skii, V. *Sov. Phys. Uspekhi* **1962**, *5*, 522.
(34) Del Riccio, J. L.; Zhang, F.; Lacey, A. R.; Kable, S. H. *J. Phys. Chem. A* **2000**, *104*, 7442.
(35) Leontidis, E.; Heinz, H.; Palewska, K.; Wallenborn, E.-U.; Suter, U. W. *J. Chem. Phys.* **2001**, *114*, 3224.
(36) Bloess, A.; Durand, Y.; Matsushita, M.; Verberk, R.; Groenen, E. J. J.; Schmidt, J. *J. Phys. Chem. A* **2001**, *105*, 3016.
(37) Aloshyna, M.; Kozankiewicz, B.; Hadad, C. M.; Snoonian, J. R.; Platz, M. S. *J. Phys. Chem. A* **2000**, *104*, 3391.
(38) Yersin, H.; Donges, D.; Humbs, W.; Strasser, J.; Sitters, R.; Glasbeek, M. *Inorg. Chem.* **2002**, *41*, 4915.
(39) Schaftenaar, G.; Noordik, J. H. *J. Comput.-Aided Mol. Des.* **2000**, *14*, 123.